# Spin-orbital liquids and insulator-metal transitions on the pyrochlore lattice

Nyayabanta Swain [1], Madhuparna Karmakar [2], and Pinaki Majumdar[1]

[1]*Harish-Chandra Research Institute (A CI of Homi Bhabha National Institute), Chhatnag Road, Jhunsi, Prayagraj 211019, India*
[2]*Centre for Quantum Science and Technology, Chennai Institute of Technology, Chennai 600037, India*

The two orbital Hubbard model, with the electrons additionally coupled to a complex magnetic background, arises in the pyrochlore molybdates. The background involves local moments Hund's coupled to the electrons, driving double exchange ferromagnetism, and antiferromagnetic (AF) tendency arising from competing superexchange. The key scales include the Hubbard repulsion and the superexchange, both of which can be tuned in these materials. They control the phase transition from a ferromagnetic metal to a spin-glass metal and then to a spin-glass (Mott) insulator. We provide a comprehensive description of the ground state of this model using an unrestricted Hartree-Fock scheme implemented via a simulated annealing procedure and establish the metal-insulator transition line for varying Hubbard interaction and superexchange. The electrons see an effective disorder, due to orbital frustration, already in the ferromagnetic phase. The disorder is further enhanced by antiferromagnetic coupling and the resulting magnetic disorder. As a result, increasing AF coupling shifts the metal-insulator transition to lower Hubbard interaction and gives it an additional "Anderson" character. We provide detailed results on the magnetic and orbital correlations, the density of states, and the optical conductivity.

## I. INTRODUCTION

The most commonly studied Mott problem [1] involves the single band Hubbard model on a bipartite lattice [2]. In such a model, typically, nesting features drive a transition [3] to an antiferromagnetic insulating state at arbitrarily weak interaction—masking the "Mott" effect. One can certainly study frustrated lattices [4], which suppress magnetic order, and there is much work on the triangular lattice Hubbard model [5–9]. This is both an important model problem [10] and also a starting point for the layered organics [11–15]. Other frustrated lattices include the Kagome [16–22] in two dimensions (2D) and the fcc and pyrochlore lattices [23–26] in three dimensions (3D). These are all harder problems than the square (or cubic) lattice since there is no longer any obvious magnetic order to simplify the correlated problem. These lattices, overall, provide an interesting variation from the bipartite case because (i) the metal-insulator transition could occur in the background of short-range magnetic correlation, and (ii) the deep Mott insulating state itself could be a spin liquid [27].

It would be vital to have experimental realizations to test out the predictions of the frustrated Mott studies. While there is a significant effort in analyzing the quasi-2D $\kappa$-BEDT organics [11–15] in terms of the triangular lattice, 3D realizations of "Hubbard physics" on a frustrated structure are rare. Materials like the manganites [28] do involve strong correlation effects (and much else) but are on a bipartite structure—with relatively simple magnetic order. The discovery of the rare-earth (R) based pyrochlores, the molybdates [29–33] $R_2Mo_2O_7$, and the iridates [34–37] $R_2Ir_2O_7$, provided

a breakthrough. Both these families show a metal-insulator transition as the rare-earth radius $r_R$ is reduced [32–35]. There are, however, key differences between these two families: (i) in terms of degrees of freedom and couplings, with respect to the Hubbard model, and (ii) the magnetic state that emerges.

Being $4d$ and $5d$ systems, respectively, both molybdates and iridates involve multiple bands. In the molybdate case this can be reduced to one itinerant electron in two degenerate orbitals. These electrons have an interorbital Hubbard repulsion and are also Hund's coupled to a $S = 1/2$ local moment at each Mo site [38]. For the iridates one can motivate the use of an effective single band model which involve strong spin-orbit coupling in addition to the Hubbard interaction [25,39]. While both families show a Mott transition, for the molybdates this happens in a somewhat spin disordered background, with no long-range order in the insulating state [23,29,30], while the iridates generally show a transition from a paramagnetic metal to an "all-in-all-out" magnetic insulator [40–42]. The frustration in the pyrochlore lattice plays a role in both these materials, but one clearly requires more than the simple Hubbard model to approach the phenomena.

This paper is focused on a detailed study of the model appropriate to the molybdates $R_2Mo_2O_7$. These exhibit ground states that vary from a ferromagnetic metal (FM-M) to a spin-glass metal (SG-M) and then a spin-glass insulator (SG-I) as the rare earth radius is reduced [43,44]. Materials with R = Nd and Sm are metallic, R = Tb, Dy, Ho, Er, and Y are insulating, and R = Gd is on the verge of the insulator-metal transition (IMT) [44,45]. The highest ferromagnetic $T_c$ is ~100 K in Nd, while the spin-glass transition temperature $T_{SG}$ is typically ~20 K [31,46,47]. The unusual features in transport include

very large residual resistivity, $\sim 10$ m$\Omega$ cm close to the metal-insulator transition [45], prominent anomalous Hall effect in metallic samples [48–52], e.g., Nd$_2$Mo$_2$O$_7$, and magnetic field driven metallization in the weakly insulating samples [53], e.g., Gd$_2$Mo$_2$O$_7$. Furthermore, it has been shown that the local structural distortion plays an important role in the stabilization of the ferromagnetic or spin-glass phases [54]. A more recent study of Mn doping of Gd and Ho molybdates in the form R$_2$(Mo$_{1-x}$Mn$_x$)$_2$O$_7$ demonstrate the strengthening of the spin-glass behavior in both systems upon doping [54]. On the other hand, Ca doping of Nd molybdate in the form (R$_{1-x}$Ca$_x$)$_2$Mo$_2$O$_7$ with $x \leqslant 0.15$ displays a robust canted ferromagnetic state. The stability of the canting angle of the Mo magnetic moments with respect to the doping is a key puzzle in the topological Hall effect observed in this material [55,56].

We will discuss the model for the molybdates in detail later, to motivate our study it suffices to mention that the active degrees of freedom include one electron per Mo in a twofold degenerate orbital, Hund's coupled to a $S = 1/2$ moment on the same ion. The electrons have on-site Hubbard repulsion ($U$) between them while the local moments have a nearest neighbor antiferromagnetic (AF) coupling $J_{AF}$. The Hund's coupling drives double exchange (DE) ferromagnetism, opposed by AF superexchange, while Hubbard repulsion promotes a Mott insulating state. Reducing $r_R$ reduces the hopping—weakening DE and also enhancing the effect of Hubbard repulsion, while increasing pressure is supposed to (mainly) affect [33] the antiferromagnetic coupling.

There are several major questions left unresolved by existing works: (1) At ambient pressure the metal-insulator and magnetic "transition" are simultaneous, is that true with increasing pressure (changing $J_{AF}$) as well? (2) Is there a "universal" quantity that dictates the metal-insulator transition (MIT) trajectory over a large pressure window? (3) What is the fate of the coupled spin-orbital state for changing pressure and rare earth radius? (4) What is the low energy spectral behavior in the vicinity of the MIT as the pressure is varied? (5) What is the quasiparticle character close to the Mott transition? (6) Can we obtain realistic thermal scales for the magnetic transitions?

We employ a real space approach, equivalent to unrestricted Hartree-Fock at zero temperature, that uses a static auxiliary orbital field to handle the Hubbard interaction. We solve the resulting "electron–local moment–orbital moment" problem via Monte Carlo based simulated annealing on the pyrochlore lattice. Within the limits of our method we address (1)–(4) of the questions posed above, and (5) and (6) elsewhere. Our main results are the following.

(i) *Phase boundaries:* The proximity of the magnetic transition and MIT in the ambient pressure molybdates is a coincidence—at weak AF coupling the metal and insulator are both ferromagnetic, while at strong AF coupling they are both spin disordered.

(ii) *Physics behind the MIT:* The shift in the critical interaction for the MIT, with applied pressure, can be understood in terms of the kinetic energy suppression driven by growing spin and orbital disorder.

(iii) *Coupled spin-orbital state:* The magnetic state is a spin ferromagnet (S-F) or a spin liquid (S-L), the orbital state is similarly an orbital ferromagnet (O-F) or an orbital liquid (O-L). We find that the low $J_{AF}$ state is mainly S-F–O-F while the large $J_{AF}$ state is S-L–O-L.

(iv) *Spectral behavior near the MIT:* The $U_c$ changes with changing $J_{AF}$, so we use a normalized frequency scale $\omega/U_c(J_{AF})$ to compare spectral features. At the MIT the larger $J_{AF}$ systems have more low energy spectral weight than the weak $J_{AF}$ case. Surprisingly, the gap edge states at large $J_{AF}$ are strongly localized, leading to an optical gap that is larger than the density of states gap, revealing the growing Anderson character of the transition with increasing $J_{AF}$.

The remainder of this paper is structured as follows. In Sec. II we discuss the static auxiliary field based Monte Carlo method in connection with the full fledged determinant quantum Monte Carlo and the unrestricted Hartree-Fock methods. This is followed by a discussion of our results in Sec. III, comprising of the ground state phase diagram, the detailed magnetic and orbital structure factors in the different phases, and the density of states and transport properties across the metal-insulator transition. We propose an effective spin only model for the fermionic system under consideration in Sec. IV and discuss the MIT in the light of this effective model. We conclude in Sec. V with pointers for experiments.

## II. MODEL AND METHOD

### A. Model

The R$_2$Mo$_2$O$_7$ structure consists of two interpenetrating pyrochlore lattices, one formed by Mo cations and the other by R. Model Hamiltonian studies ignore the orbitals on R and oxygen, focusing instead on the orbitals on Mo. The Mo atom has octahedral oxygen coordination, the resulting crystal field splits the fivefold degenerate Mo $4d$ states into doubly degenerate $e_g$ and triply degenerate $t_{2g}$ manifolds, and a trigonal distortion splits the $t_{2g}$ further into a nondegenerate $a_{1g}$ and a doubly degenerate $e'_g$. The hopping between Mo orbitals at different sites is mediated by the intervening oxygen. The Mo cation is nominally tetravalent and has two electrons on average. The deeper $a_{1g}$ state behaves like a local moment, and the single electron in the two $e'_g$ orbitals is the "itinerant" degree of freedom [38]. The $e_g$ state remains unoccupied.

There are additional small scales, related to bond distortions, etc., that are responsible for the spin freezing phenomena [57,58]. We ignore them for the time being. Also, the moments on R can be relevant when studying effects like spin chirality induced anomalous Hall effect [48–52]. We do not include these moments in our model.

We study the following model [59], in the parameter regimes described below:

$$H = \sum_{\langle ij \rangle, \alpha\beta, \sigma} t_{ij}^{\alpha\beta} c_{i\alpha\sigma}^\dagger c_{j\beta\sigma} - J_H \sum_{i,\alpha} \mathbf{S}_i \cdot c_{i\alpha\sigma}^\dagger \vec{\sigma}_{\sigma\sigma'} c_{i\alpha\sigma'}$$

$$+ J_{AF} \sum_{\langle ij \rangle} \mathbf{S}_i \cdot \mathbf{S}_j + \sum_{i,\alpha\beta\alpha'\beta'}^{\sigma,\sigma'} U_{\alpha\beta}^{\alpha'\beta'} c_{i\alpha\sigma}^\dagger c_{i\beta\sigma'}^\dagger c_{i\beta\sigma'} c_{i\alpha\sigma}.$$

The first term is the kinetic energy, involving nearest neighbor intra- and interorbital $e'_g$ hopping. The second term is the Hund's coupling between the $a_{1g}$ local moment $\mathbf{S}_i$ and the

$e'_g$ electrons, $J_{\mathrm{AF}}$ is the AF superexchange coupling between local moments at neighboring sites on the pyrochlore lattice, and the $U$ represent on-site $e'_g$ Coulomb matrix elements.

To simplify the computational problem we treat the localized spins $\mathbf{S}_i$ as classical unit vectors, absorbing the size $S$ in the magnetic couplings. We will comment on the limitations of this approximation later. Also, to reduce the size of the Hilbert space we assume that $J_H/t \gg 1$, where $t$ is the typical hopping scale, so that only the locally "spin aligned" fermion state is retained. In this local basis the hopping matrix elements are dictated by the orientation of the $\mathbf{S}_i$ on neighboring sites. This leads to the simpler model:

$$H = \sum_{\langle ij \rangle, \alpha\beta} \tilde{t}_{ij}^{\alpha\beta} \tilde{c}_{i\alpha}^{\dagger} \tilde{c}_{j\beta} + J_{\mathrm{AF}} \sum_{\langle ij \rangle} \mathbf{S}_i \cdot \mathbf{S}_j + U \sum_i^{\alpha\neq\beta} n_{i\alpha} n_{i\beta},$$

where the fermions are now "spinless." and $U > 0$ is the interorbital Hubbard repulsion. The effective hopping is determined by the orientation of the localized spins $\mathbf{S}_i = (\sin\theta_i \cos\phi_i, \sin\theta_i \sin\phi_i, \cos\theta_i)$, as $t_{ij}^{\alpha\beta} = [\cos\frac{\theta_i}{2} \cos\frac{\theta_j}{2} + \sin\frac{\theta_i}{2} \sin\frac{\theta_j}{2} e^{-i(\phi_i-\phi_j)}]t^{\alpha\beta}$, with $t^{11} = t^{22} = t$ and $t^{12} = t^{21} = t'$. We set $t' = 1.5t$ as is appropriate for these kinds of orbitals [38].

The first two terms represent fermions in a classical spin background and the resulting magnetic phase competition has been studied on a pyrochlore [60]. While these results are interesting, they miss out on the large correlation scale $U$ that drives the Mott transition. One option is to treat the model within dynamical mean field theory (DMFT) [61], but then the spatial character crucial to the pyrochlore lattice is lost.

The current paper is focused on the ground state but we discuss our general strategy for solving the finite temperature problem below. This will describe the simulated annealing scheme for arriving at the ground state.

## B. Method

We handle the problem in real space as follows: (i) We use a Hubbard-Stratonovich (HS) [62–64] decomposition that decouples $U n_{i\alpha} n_{i\beta}$ in terms of an auxiliary orbital variable $\mathbf{\Gamma}_i(\tau)$, coupling to the electronic orbital moment $\mathbf{O}_i = \sum_{\mu\nu} c_{i\mu}^{\dagger} \vec{\sigma}_{\mu\nu} c_{i\nu}$, and a scalar field $\Phi_i(\tau)$ coupling to the electronic density $n_i$ at each site. The Matsubara frequency versions of these fields are $\mathbf{\Gamma}_{i,n}$ and $\Phi_{i,n}$, where $\Omega_n = 2\pi nT$ is a bosonic frequency. (ii) An exact treatment of the resulting functional integral, see below, requires determinant quantum Monte Carlo (DQMC)—computing a fermion determinant $D(\mathbf{\Gamma}_{i,n}, \Phi_{i,n}, \mathbf{S}_i)$ iteratively as the "weight factor" for auxiliary field configurations. Fermion Green's functions would be computed on the equilibrium $\{\mathbf{\Gamma}, \Phi, \mathbf{S}\}$ backgrounds.

The DQMC implementation, which we will approximate, takes the following route. The partition function is written as a functional integral over Grassmann fields $\psi_{i\alpha}(\tau)$ and $\bar{\psi}_{i\alpha}(\tau)$:

$$Z = \int \mathcal{D}\psi \mathcal{D}\bar{\psi} \mathcal{D}\mathbf{S} e^{-\int_0^\beta d\tau \mathcal{L}(\tau)},$$

$$\mathcal{L}(\tau) = \sum_{\langle ij \rangle, \alpha\beta} \left\{ \bar{\psi}_{i\alpha} \left[ (\partial_\tau - \mu)\delta_{ij}\delta_{\alpha\beta} + \tilde{t}_{ij}^{\alpha\beta} \right] \psi_{j\beta} \right\}$$

$$+ U \sum_{i,\alpha\neq\beta} \bar{\psi}_{i\alpha} \psi_{i\alpha} \bar{\psi}_{i\beta} \psi_{i\beta} + J_{\mathrm{AF}} \sum_{\langle ij \rangle} \mathbf{S}_i \cdot \mathbf{S}_j.$$

The quartic term is "decoupled" exactly via a Hubbard-Stratonovich transformation

$$e^{U \bar{\psi}_{i\alpha} \psi_{i\alpha} \bar{\psi}_{i\beta} \psi_{i\beta}} = \int \frac{d\Phi_i d\mathbf{\Gamma}_i}{4\pi^2 U} e^{(i\Phi_i n_i - \mathbf{\Gamma}_i \cdot \mathbf{O}_i + \frac{\Phi_i^2}{U} + \frac{\Gamma_i^2}{U})},$$

where $\Phi_i(\tau)$ and $\mathbf{\Gamma}_i(\tau)$ are two auxiliary fields: $\Phi_i(\tau)$ coupling to charge density $n_i = n_{i\alpha} + n_{i\beta}$, and $\mathbf{\Gamma}_i(\tau)$ coupling to the orbital variable $\mathbf{O}_i = \sum_{\mu\nu} \bar{\psi}_{i\mu} \vec{\sigma}_{\mu\nu} \psi_{i\nu}$. This leads to

$$Z = \int \mathcal{D}\psi \mathcal{D}\bar{\psi} \mathcal{D}\mathbf{S} \prod_i \frac{d\Phi_i d\mathbf{\Gamma}_i}{4\pi^2 U} e^{-\int_0^\beta d\tau \mathcal{L}(\tau)},$$

$$\mathcal{L}(\tau) = \mathcal{L}_0(\tau) + \mathcal{L}_{\mathrm{int}}(\tau) + \mathcal{L}_{\mathrm{cl}}(\tau),$$

$$\mathcal{L}_0(\tau) = \sum_{\langle ij \rangle, \alpha\beta} \left\{ \bar{\psi}_{i\alpha} \left[ (\partial_\tau - \mu)\delta_{ij}\delta_{\alpha\beta} + \tilde{t}_{ij}^{\alpha\beta} \right] \psi_{j\nu} \right\},$$

$$\mathcal{L}_{\mathrm{int}}(\tau) = \sum_i^{\alpha\beta} \left\{ i\Phi_i \bar{\psi}_{i\alpha} \psi_{i\beta} \delta_{\alpha\beta} - \mathbf{\Gamma}_i \cdot \bar{\psi}_{i\alpha} \vec{\sigma}_i \psi_{i\beta} \right\},$$

$$\mathcal{L}_{\mathrm{cl}}(\tau) = \sum_i \left\{ \frac{\Phi_i^2}{U} + \frac{\Gamma_i^2}{U} \right\} + J_{\mathrm{AF}} \sum_{\langle ij \rangle} \mathbf{S}_i \cdot \mathbf{S}_j.$$

Since the fermions are now quadratic the $\int \mathcal{D}\Psi..$ integrals can be formally performed to generate the effective action for the background fields:

$$Z \sim \int \mathcal{D}\Phi \mathcal{D}\mathbf{\Gamma} \mathcal{D}\mathbf{S} e^{-S_{\mathrm{eff}}\{\Phi,\mathbf{\Gamma},\mathbf{S}\}},$$

$$S_{\mathrm{eff}} = \log \mathrm{Det}[\mathcal{G}^{-1}\{\Phi, \mathbf{\Gamma}, \mathbf{S}\}] + \int_0^\beta d\tau \mathcal{L}_{\mathrm{cl}}(\tau).$$

In the expression above, $\mathcal{G}$ is the electron Green's function in a $\{\Phi, \mathbf{\Gamma}, \mathbf{S}\}$ background.

Now the options. (1) Determinant quantum Monte Carlo would proceed by using $S_{\mathrm{eff}}$ as the "weight" for the background configurations, and compute electron properties on these after equilibration. (2) Mean field theory would assume the fields to be time independent, replace them by their mean values, and minimize the free energy. (3) A *static path approximation* to $Z$ again assumes the fields to be time independent, but samples over spatial fluctuations.

We adopt method (3), which is computationally simpler than DQMC but much more sophisticated than MFT at finite temperature. So we (i) neglect the imaginary time dependence of $\Phi_i$ and $\mathbf{\Gamma}_i$, i.e., retain only the zero Matsubara frequency modes of these fields, and (ii) replace $\Phi_i$ by its saddle point value $\langle \Phi_i \rangle = (U/2)\langle n_i \rangle = U/2$, since the important low energy fluctuations arise from the $\mathbf{\Gamma}_i$. The electron is now subject to *static* background fields so the partition function can be written as a trace over an effective "Hamiltonian," rather than require an effective "action." Specifically,

$$H_{\mathrm{eff}}\{\mathbf{\Gamma}_i, \mathbf{S}_i\} = -\frac{1}{\beta} \log \mathrm{Tr} e^{-\beta H_{\mathrm{el}}} + H_{\mathrm{AF}} + \frac{1}{U} \sum_i \mathbf{\Gamma}_i^2,$$

$$H_{\mathrm{el}} = \sum_{ij}^{\alpha\beta} \tilde{t}_{ij}^{\alpha\beta} c_{i\alpha}^{\dagger} c_{j\beta} - \tilde{\mu} \sum_i n_i - \sum_i \mathbf{\Gamma}_i \cdot \mathbf{O}_i,$$

with $\tilde{\mu} = \mu - U/2$ and $H_{AF}$ the Heisenberg term. For convenience we redefine $\Gamma_i \rightarrow \frac{U}{2}\Gamma_i$, so that the $\Gamma_i$ is dimensionless. This leads to the effective electronic Hamiltonian used in the text:

$$H_{el} = \sum_{ij}^{\alpha\beta} \tilde{t}_{ij}^{\alpha\beta} c_{i\alpha}^{\dagger} c_{j\beta} - \tilde{\mu} \sum_i n_i - \frac{U}{2} \sum_i \Gamma_i \cdot O_i.$$

The localized spin and orbital moment configurations follow the distribution

$$P\{\mathbf{S}_i, \Gamma_i\} \propto \mathrm{Tr}_{cc^{\dagger}} e^{-\beta H_{eff}}.$$

This overall approach has been used in the nuclear many-body problem [65,66], superconductivity [67–70], etc., and by us in other studies of the Mott problem before [71,72].

There are regimes where some analytic progress can be made, as we discuss later, but our results are based on a Monte Carlo solution of the model above—generating the equilibrium configuration for the $\{\mathbf{S}_i, \Gamma_i\}$ through iterative diagonalization of $H_{eff}$. We start with high temperature $\sim 0.5t$, higher than any transition temperature in the problem, and reduce it to $T = 0.001t$ to access the ground state properties. To access large system sizes within reasonable time we use a cluster algorithm [73] for estimating the update cost. Results in this paper are for a $6 \times 6 \times 6$ pyrochlore lattice of $\sim 800$ atoms.

A couple of comments on the $T \rightarrow 0$ limit of our method which reduces to unrestricted Hartree-Fock in the magnetic channel. Traditionally, Hartree-Fock calculations impose a certain pattern on the order parameter and minimize with respect to the amplitude. On a frustrated geometry it is not clear on what pattern to impose so we vary with respect to the full set $\{\mathbf{S}_i, \Gamma_i\}$. The resulting state turns out to be disordered but correlated, and leads to a nontrivial electronic spectrum.

### C. Observables

From the equilibrium configurations obtained at the end of annealing we calculate the following averaged quantities (angular brackets represent thermal average over MC configurations): (i) Magnetic and orbital structure factors are

$$S_{mag}(\mathbf{q}) = \frac{1}{N^2} \sum_{ij} \langle \mathbf{S}_i \cdot \mathbf{S}_j \rangle e^{i\mathbf{q} \cdot (\mathbf{r}_i - \mathbf{r}_j)},$$

$$S_{orb}(\mathbf{q}) = \frac{1}{N^2} \sum_{ij} \langle \Gamma_i \cdot \Gamma_j \rangle e^{i\mathbf{q} \cdot (\mathbf{r}_i - \mathbf{r}_j)}.$$

(ii) The size distribution of the orbital field is computed as

$$P(\Gamma) = \frac{1}{N} \sum_i \langle \delta(\Gamma - |\Gamma_i|) \rangle.$$

(iii) The electronic density of states is

$$N(\omega) = \frac{1}{N} \sum_n \langle \delta(\omega - \epsilon_n) \rangle,$$

where $\epsilon_n$ are single particle eigenvalues in an equilibrium configuration. (iv) The optical conductivity is

$$\sigma_{xx}(\omega) = \frac{\sigma_0}{N} \left\langle \sum_{n,m} \frac{f(\epsilon_n) - f(\epsilon_m)}{\epsilon_m - \epsilon_n} |J_x^{nm}|^2 \delta(\omega - E_{mn}) \right\rangle,$$
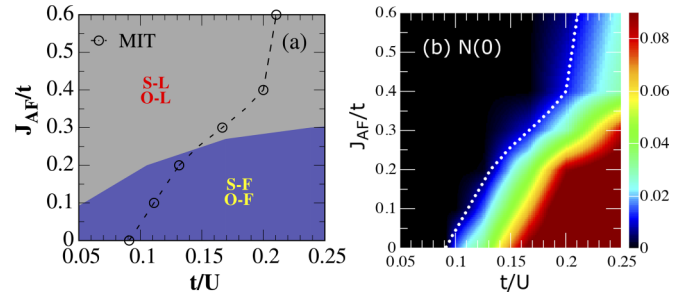


FIG. 1. (a) Ground state phase diagram showing the metal-insulator transition (MIT) boundary in the $t/U$ and $J_{AF}/t$ plane. We label the various magnetic phases as spin ferromagnet (S-F) and spin liquid (S-L). The two orbital phases are labeled as orbital ferromagnet (O-F) and orbital liquid (O-L). The detailed characterization of these phases is mentioned in the text. (b) The density of states at the Fermi level $N(0)$ for varying $t/U$ and $J_{AF}/t$. The dotted line corresponds to MIT. $N(0)$ vanishes in the insulating phase at weak $J_{AF}/t$. However, it retains a small nonzero value at large $J_{AF}/t$, an indication of frustration induced Anderson localization behavior (discussed later).

where $J_x^{nm}$ is $\langle n|J_x|m \rangle$ and the current operator is given by

$$J_x = -i \sum_{i,\alpha\beta} \left[ (\tilde{t}_{i,i+\hat{x}}^{\alpha\beta} c_{i,\alpha}^{\dagger} c_{i+\hat{x},\beta} - \mathrm{H.c.}) \right].$$

$E_{mn} = \epsilon_m - \epsilon_n$, $f(\epsilon_n)$ is the Fermi function, and $\epsilon_n$ and $|n\rangle$ are the single particle eigenvalues and eigenstates of $H_{el}$, respectively. The conductivity is in units of $\sigma_0 = e^2/(\hbar a_0)$, where $a_0$ is the lattice constant. (v) The DC conductivity is obtained as a low frequency average of the optical conductivity over a window $\Omega = 0.05t$,

$$\sigma_{DC} = \frac{1}{\Omega} \int_0^{\Omega} d\omega \, \sigma_{xx}(\omega),$$

and the resistivity $\rho = 1/\sigma_{DC}$.

### III. RESULTS

#### A. Phase diagram

Figure 1(a) shows the ground state of the model for varying $U/t$ and $J_{AF}/t$, while Fig. 1(b) shows $N(0)$, the density of states at the Fermi level, over the same parameter space.

First the notation: We characterize phases in terms of their spin and orbital character, S-L is spin liquid and S-F is a spin ferromagnet. Similarly, O-L is orbital liquid, etc. These phases also need to be specified in terms of their transport character. To avoid a cluttered picture we have simply shown the metal-insulator boundary in the $t/U$-$J_{AF}/t$ plane, the metal/insulator aspect can be inferred from it. The metal-insulator transition can be located from the vanishing of $N(0)$, and also from a calculation of the DC conductivity.

When $J_{AF} = 0$ there is a metal-insulator transition at $U_c \sim 11t$ from a ferromagnetic metal to a *ferromagnetic insulator*. When the superexchange is moderate, $J_{AF} \sim 0.2t$, there is strong competition between ferromagnetism (S-F, mediated by double exchange) and antiferromagnetic tendency. As a result there is a crossover from S-F to spin disordered (S-L) behavior with increasing $U/t$ roughly around the MIT,
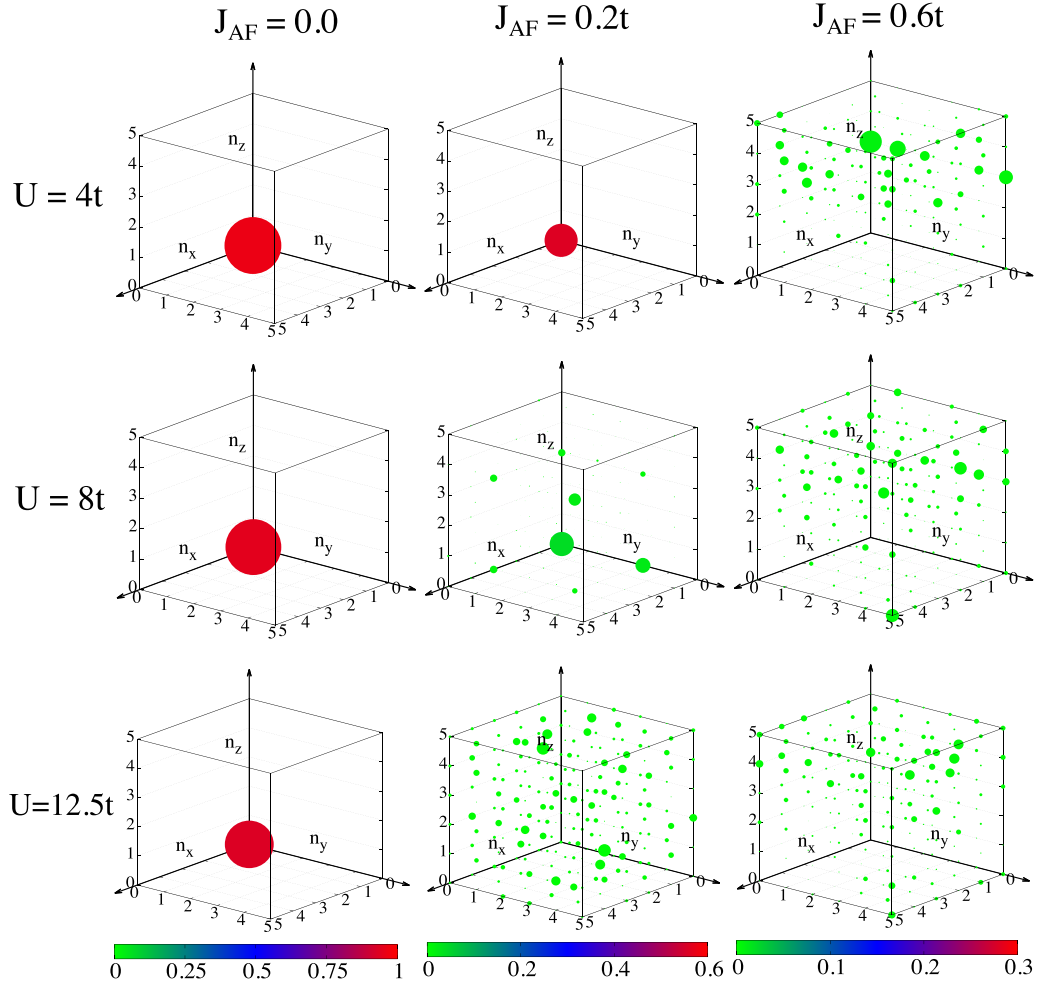
FIG. 2. Spin structure factor $S_{mag}(\mathbf{q})$ at $T = 0$ for $U/t = 4$, 8, and 12.5 for each of $J_{AF}/t = 0$ (left column), 0.2 (middle column), and 0.6 (right column). We use the notation $\mathbf{q} = \frac{2\pi}{L}(n_x, n_y, n_z)$, where $n_i$'s are integers and $0 \leqslant n_i < L$. In our calculation $L = 6$. The size of a dot signifies the relative weight at a given $\mathbf{q}$ while its color represents the actual magnitude of $S_{mag}(\mathbf{q})$. The presence of dominant weight at some $\mathbf{q}$, in these cases $\mathbf{q} = (0, 0, 0)$ indicates magnetic order phase, while the "random" but correlated patterns indicate a spin liquid.

although weak ferromagnetism survives in the insulator. For strong superexchange $J_{AF} \gtrsim 0.5t$, the antiferromagnetic tendency suppresses ferromagnetism completely and, as we will show, there is no magnetization at any $U/t$. We have a spin liquid (S-L) state at all $U/t$. In this large $J_{AF}$ limit, a relatively weak Hubbard repulsion $U \sim 5t$ is enough to drive the metal-insulator transition.

### B. The magnetic state

A detailed understanding of the magnetic state is provided by the magnetic structure factor $S_{mag}(\mathbf{q})$ computed in the optimized background. It highlights not only long-range order, in terms of prominent peaks in $\mathbf{q}$ space, but also possible correlations in the disordered state when there is no long-range order.

Figure 2 shows $S_{mag}(\mathbf{q})$ for three different superexchange couplings and for three $U$'s in each case. The $U$'s are chosen so that they capture the metal, insulator, and crossover regime for all three values of $J_{AF}$.

For $J_{AF} = 0$ there is no magnetic phase competition. At $U = 4t$, $S_{mag}(\mathbf{q})$ has dominant weight at $\mathbf{q} = (0, 0, 0)$ describing the ferromagnetic order promoted by double exchange.

The magnetization is $\gtrsim 0.95$ (limited by our annealing process) and the structure factor peak is $\sim 0.9 \sim M^2$. As the column shows, this result does not depend on $U$, suggesting that even deep in the Mott insulator one would obtain a saturated ferromagnetic state. The $T_c$'s would of course differ, since the stiffness of the FM state depends on the kinetic energy—which is $U$ dependent.

For $J_{AF} = 0.2t$, $S_{mag}(\mathbf{q})$ has a large weight at $\mathbf{q} = (0, 0, 0)$ at $U = 4t$, as in the first row, but at $U = 8t$ the peak, although still at $(0,0,0)$, has diminished weight $\sim 0.1$. The metal-insulator transition occurs around $U \sim 8t$ and by the time $U = 12.5t$ (last row) $S_{mag}$ does not have any prominent peaks at any $\mathbf{q}$. The superexchange coupling overcomes the kinetic energy gain from DE but the pyrochlore structure prevents AF ordering.

For $J_{AF} = 0.6t$, $S_{mag}(\mathbf{q})$ the weight is spread over all $\mathbf{q}$ but in a correlated manner, indicative of a spin liquid phase.

### C. The orbital state

To have an idea of the underlying orbital state, we calculate the orbital structure factor $S_{orb}(\mathbf{q})$. Figure 3 shows the
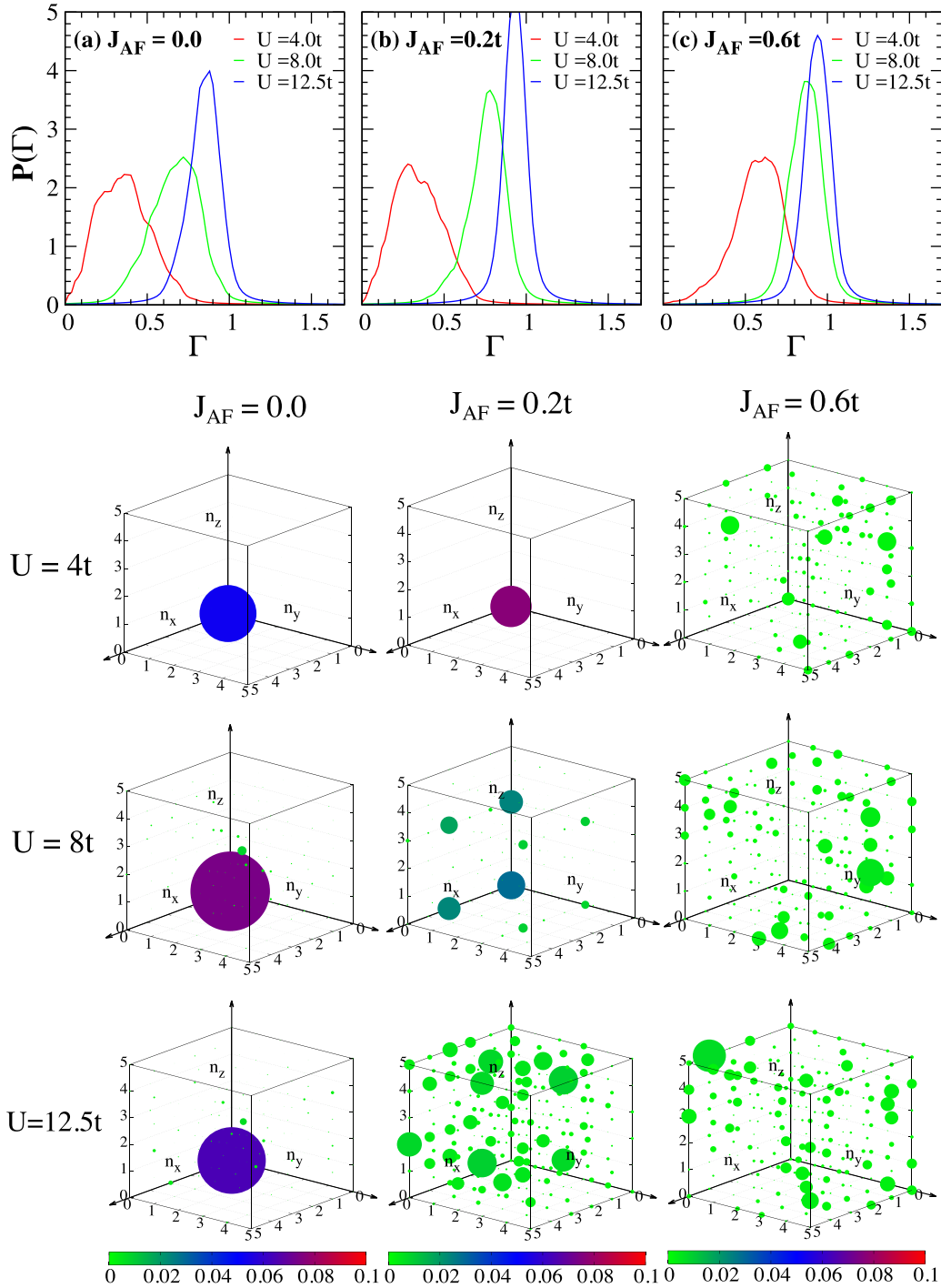
FIG. 3. (Top row) Ground state size distribution of the orbital field $P(\Gamma)$ for $J_{AF} = 0, 0.2t$, and $0.6t$ for the indicated $U$ values. (Remaining rows) Orbital structure factor at $T = 0$ for $U/t = 4, 8$, and $12.5$ for each of $J_{AF}/t = 0$ (left column), $0.2$ (middle column), and $0.6$ (right column). We use the same convention as described in Fig. 2. The size of a dot signifies the relative weight at a given $\mathbf{q}$ while its color represents the actual magnitude of $S_{orb}(\mathbf{q})$. The presence of dominant weight at some $\mathbf{q}$ indicates an orbital ordered phase, otherwise a disordered phase.

structure factor for the three superexchange couplings. For $J_{AF} = 0$ we see $S_{orb}(\mathbf{q})$ has dominant weight at $\mathbf{q} = (0, 0, 0)$ describing the orbital ferro (O-F) ordering. For $J_{AF} = 0.2t$, $S_{orb}(\mathbf{q})$ has dominant weight at $\mathbf{q} = (0, 0, 0)$ for $U = 4t$ and $8t$ (O-F ordering), and an orbital liquid state for $U = 12.5t$. For $J_{AF} = 0.6t$, $S_{orb}(\mathbf{q})$ has weight spread over all $\mathbf{q}$ indicating an orbital liquid state.

### D. Density of states

Figure 4 shows the ground state density of states (DOS) for various interaction strengths for the three regimes of superexchange interaction of our phase diagram. We can see that for $U < U_c$, the DOS has a finite weight at the Fermi energy, and for $U \geqslant U_c$, the DOS has a gap in the spectrum. As $U \to U_c$, the DOS develops a prominent dip at the Fermi
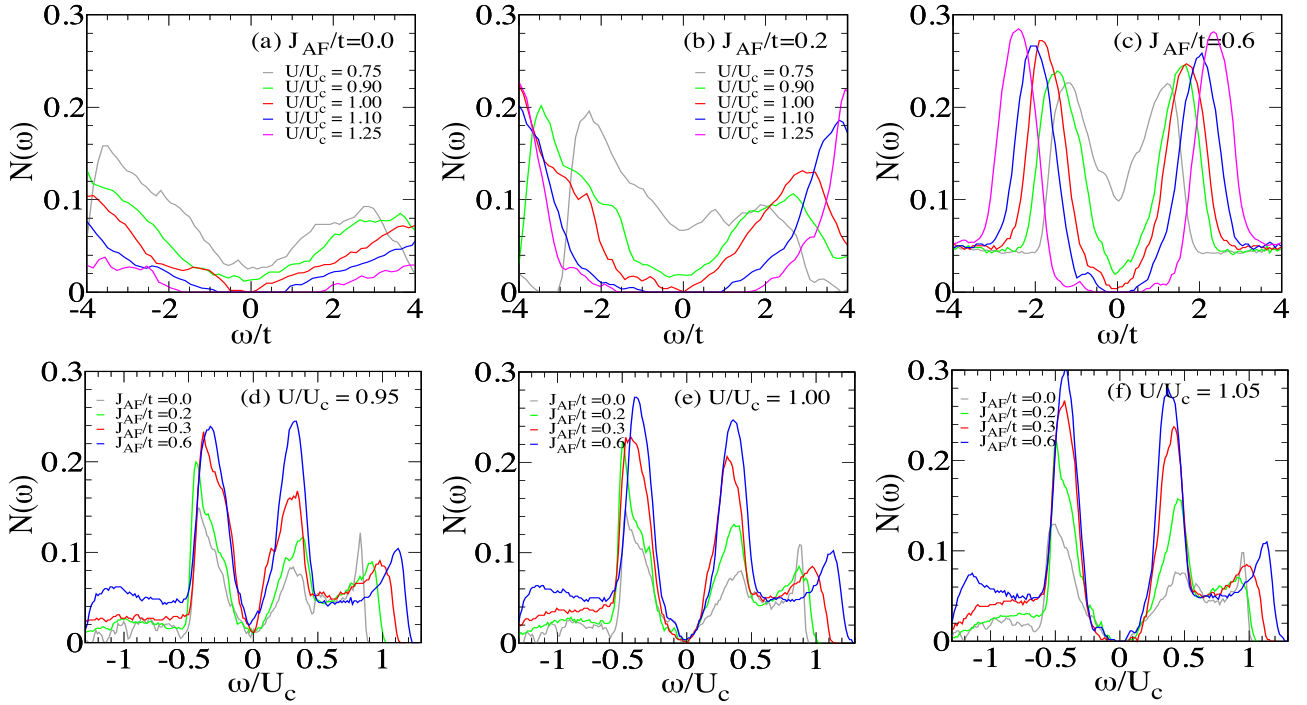
FIG. 4. (a)–(c) Ground state density of states (DOS) for $J_{AF} = 0$, $0.2t$, and $0.6t$ for different $U/U_c$. (d)–(f) Ground state DOS for $U/U_c = 0.95$, $1.0$, and $1.05$, on a normalized frequency scale, for the indicated $J_{AF}$ values.

energy, a signature of the pseudogap (PG) phase. We can understand this in the following way. The band ($U = 0$) limit of this model is a metal, with finite DOS and a peak at the Fermi level. Inclusion of the interorbital interaction ($U$) leads to the emergence of orbital moments $\mathbf{\Gamma}_i$, with the size of the orbital moment $|\mathbf{\Gamma}_i|$ determined by the strength of $U$. For $U < U_c$, we have $|\mathbf{\Gamma}_i| \ll \Gamma_{sat} = 1$ (see Fig. 8, discussed later) The presence of these orbital moments reduce the DOS at the Fermi level. As $U \to U_c$, $|\mathbf{\Gamma}_i|$ increases monotonically and for $U \gg U_c$ it saturates to the atomic value $|\mathbf{\Gamma}_i| = 1$. The presence of large orbital moments for $U \geqslant U_c$ leads to the opening of a gap in the DOS. From our calculation we estimate that for $J_{AF} = 0$, $U_c = 11.0t$, for $J_{AF} = 0.2t$, $U_c = 7.6t$, and for $J_{AF} = 0.6t$, $U_c = 5.0t$. The superexchange interaction favors the Mott-insulating phase.

The lower set of panels in Fig. 4 show the DOS near the MIT for fixed ratios of $U/U_c(J_{AF})$. Within each panel the $J_{AF}$ is varied to probe if the spectral behavior changes with changing AF coupling, after factoring out the effect of $U_c$ change by normalizing the frequency axis by $U_c$. Our primary observation is that increasing $J_{AF}$ leads to enhanced low energy DOS for a fixed ratio $U/U_c$. We attribute this to the increased spin and orbital disorder in the larger $J_{AF}$ situation—leading to an increasing "Anderson-Mott" character of the metal-insulator transition. We have computed the inverse participation ratio (IPR) for states as $J_{AF}$ is increased and found increasing localization. We discuss those results later.

**E. Optics and transport**

Figure 5 shows the optical conductivity $\sigma(\omega)$ in the ground state for various interaction strengths and three regimes of superexchange interaction of our phase diagram.

The band ($U = 0$) limit of the model has finite DOS at the Fermi level. As a result $\sigma(\omega)$ shows a Drude peak in this limit. Interorbital interaction ($U$) leads to the emergence of orbital moments $\mathbf{\Gamma}_i$. For $U < U_c$, we have $|\mathbf{\Gamma}_i| \ll \Gamma_{sat} = 1$. Increasing size of these orbital moments leads to a suppressed Drude response, and $\sigma(\omega)$ peak shifts to higher frequencies, indicating an increase in the insulating tendency of the system.

$|\mathbf{\Gamma}_i|$ increases monotonically with increasing $U$ and for $U \gg U_c$ it saturates to the atomic value $|\mathbf{\Gamma}_i| = 1$. Beyond $U_c$ there is an optical gap in $\sigma(\omega)$. From our calculation we find that the $U_c$'s for different superexchange scales are consistent with those obtained from the DOS results.

The lower set of panels in Fig. 5 show the optical conductivity near the MIT for fixed ratios of $U/U_c(J_{AF})$. Within each panel the $J_{AF}$ is varied to probe if $\sigma(\omega)$ changes with changing AF coupling, after factoring out the effect of $U_c$ change by normalizing the frequency axis by $U_c$. Our primary observation is the increase in the low frequency spectral weight at a fixed $U/U_c$ as $J_{AF}$, and the associated background disorder increases.

We show the optical gap $\Delta$ in Fig. 6(a). It is clearly seen that $\Delta = 0$ for $U < U_c$ and it increases monotonically for $U \geqslant U_c$. Figure 6(b) shows the variation of the residual DC resistivity $\rho(T = 0)$ with $U/t$ for different superexchange values. The finite $\rho(0)$ for $U < U_c$ can be understood by the scattering of electrons from the (small) orbital moments. For $U \geqslant U_c$, the (large) orbital moments lead to an opening of a Mott gap which manifests as $\rho(0) \to \infty$. These behaviors are seen in Fig. 6.

Figure 7 shows the DC conductivity $\sigma_{DC}$ from our calculation in the $t/U$-$J_{AF}/t$ plane. We observe $\sigma_{DC}$ vanishing as $U \geqslant U_c$. This also allows us to roughly estimate the MIT boundary.
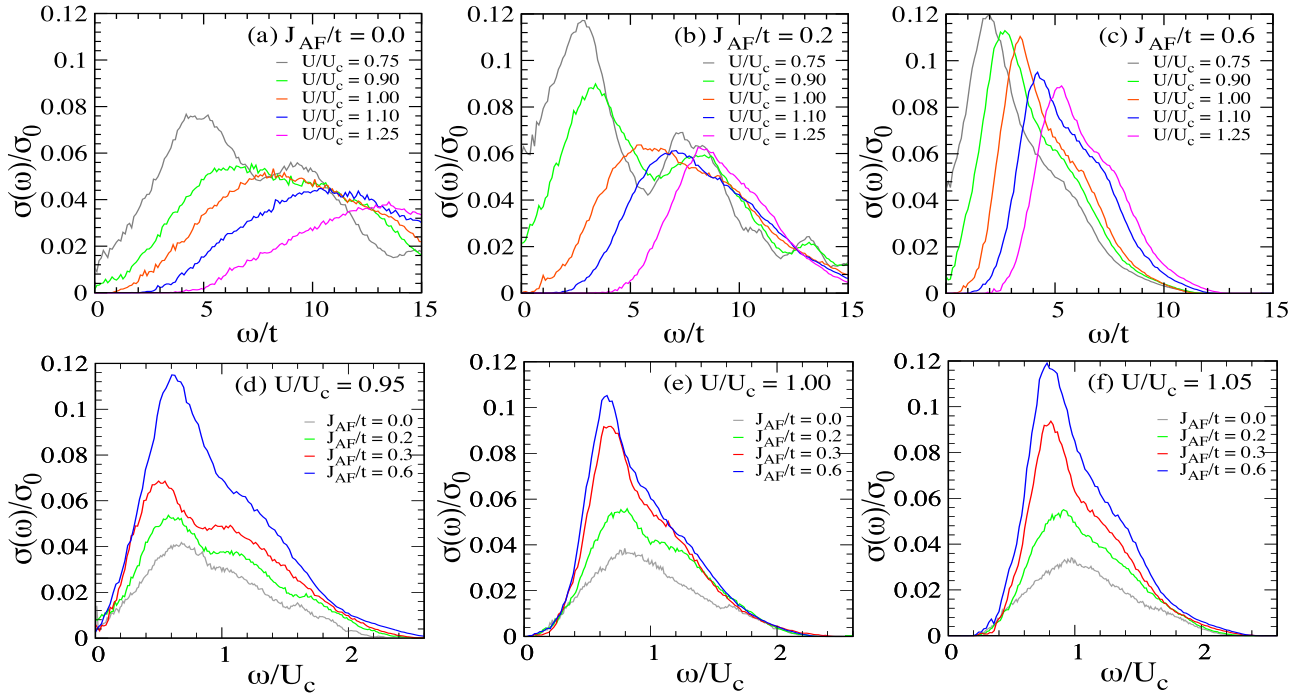
FIG. 5. (a)–(c) Ground state optical conductivity for $J_{AF} = 0$, $0.2t$, and $0.6t$ for different $U/U_c$. (d)–(f) Ground state optical conductivity for $U/U_c = 0.95$, 1.0, and 1.05, on a normalized frequency scale, for the indicated $J_{AF}$ values.

In Fig. 8(a) we highlight the behavior of the magnetization ($M$) in the ground state. We find that at $J_{AF} = 0$ the system has saturated magnetization ($M = 1$) at all $U$ values, irrespective of the metallic or insulating character. On the other hand, for $J_{AF} \gtrsim 0.5t$, the magnetization is vanishingly small ($M \sim 0$) for the entire $U$ range probed in our study. For intermediate $J_{AF}$ values, the magnetization displays a rapid crossover around a scale $U_{mag}(J_{AF})$ that is close to but not quite the metal-insulator transition point $U_c(J_{AF})$. This is an indication of distinct energy scales governing the magnetic transition and the Mott transition in our model.
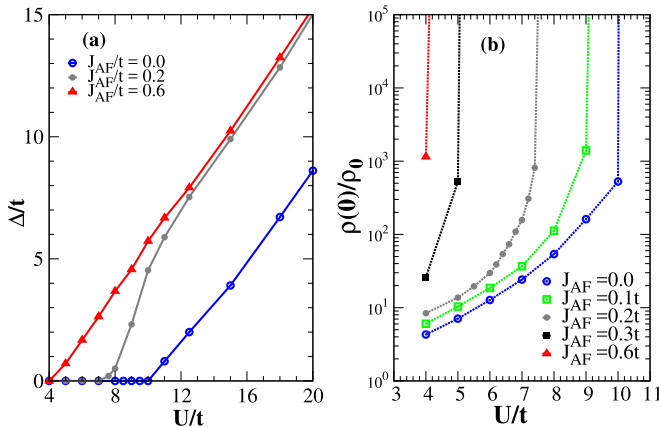
In Fig. 8(b) we show the behavior of average orbital moment $\Gamma_{avg} = 1/N \sum_i |\Gamma_i|$ in the ground state. For $U/t \to \infty$, the orbital moment $\to 1$, as one expects in the atomic limit. The approach to this asymptote is faster at larger $J_{AF}$ values. On the other hand, the $U \to 0$ behavior is dictated by the electronic band structure, and change in the magnetic state with $J_{AF}$. In Figs. 8(c) and 8(d) we show the overall variation of $M$ and $\Gamma_{avg}$ in the ground state, in the $J_{AF}/t$ and $t/U$ plane. It can be seen that the boundary separating the ferromagnetic and spin-liquid phases, and the MIT boundary separating the
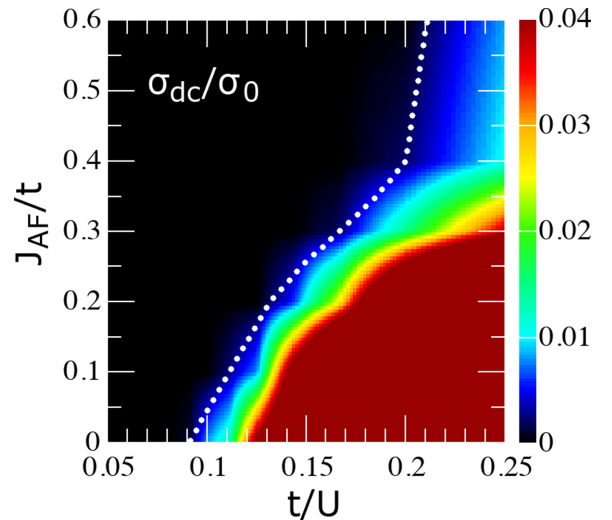


FIG. 6. (a) Variation of the optical gap ($\Delta/t$) with $U/t$ for different $J_{AF}/t$ values. (b) The variation of the residual resistivity $\rho(T = 0)$ with $U/t$ for different $J_{AF}/t$ values. The normalizing scale is $\rho_0 = \hbar/e^2$.



FIG. 7. Ground state DC conductivity $\sigma_{DC}$ for varying $t/U$ and $J_{AF}/t$. The normalizing scale is $\sigma_0 = e^2/\hbar$. The MIT boundary can be thought of as the vanishing of $\sigma_{DC}$, with increasing $U/t$ values.
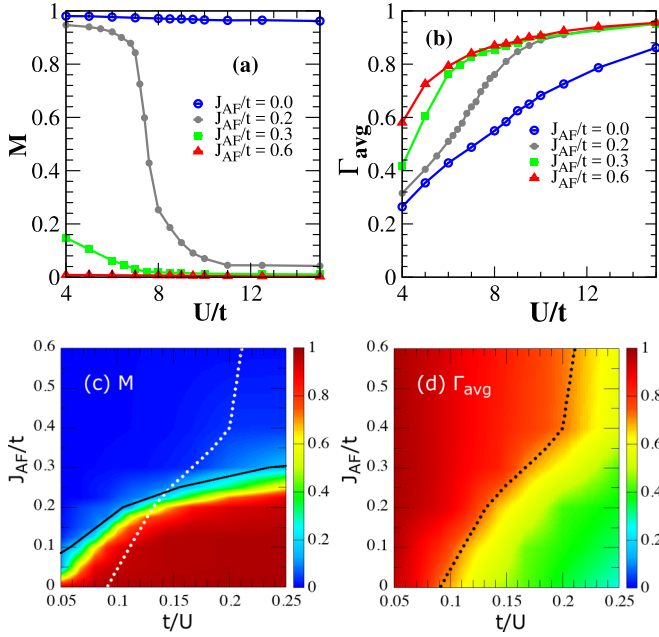
FIG. 8. Magnetization ($M$) and average orbital moment ($\Gamma_{\text{avg}}$) in the ground state. (a) $U/t$ dependence of $M$ at $J_{\text{AF}} = 0$ indicates that the system has $M = 1$ at all $U$, irrespective of the metal/insulator character, and for $J_{\text{AF}} \gtrsim 0.5t$, $M \sim 0$ for the entire $U$ window probed. At intermediate $J_{\text{AF}}$, $M$ shows a rapid crossover around a scale $U_{\text{mag}}(J_{\text{AF}})$ that is close to but not quite the metal-insulator transition point $U_c(J_{\text{AF}})$. (b) For $U/t \to \infty$, the orbital moment, $\Gamma_{\text{avg}} \to 1$, as expected in the atomic limit. The approach to this asymptote is faster at larger $J_{\text{AF}}$. The $U \to 0$ behavior is dictated by the band structure, and change in the magnetic state with $J_{\text{AF}}$. (c) and (d) Overall variation of $M$ and $\Gamma_{\text{avg}}$ in the $J_{\text{AF}}/t$ and $t/U$ plane. The dashed line is the MIT boundary separating the metallic and insulating regimes.

metallic and insulating regimes, are distinct ones. We discuss the detailed nature of this interplay next.

## IV. DISCUSSION

To get a feel for the changing magnetic state and the shifting MI transition point, it is useful to examine an approximate effective "spin only" model. Consider the bond kinetic energy in a spin configuration $\{\mathbf{S}_i\}$. It is the product of an electronic average and a modulated hopping both of which depend on $\{\mathbf{S}_i\}$. The dependence of the spin overlap factor is explicit, it is simply $\sqrt{(1 + \mathbf{S}_i \cdot \mathbf{S}_j)/2}$. The electronic average does not have an obvious expression in terms of the spins but, as a starting approximation, we can replace $\langle c_{i\alpha}^\dagger c_{j\beta} \rangle$ by its thermal average [74]. The thermal average, please note, is not a spin configuration dependent quantity.

Under this assumption the kinetic energy term can be approximated as below, and added to the AF term:

$$H_{\text{eff}}\{\mathbf{S}\} \approx \sum_{ij} D_{ij}\sqrt{(1 + \mathbf{S}_i \cdot \mathbf{S}_j)/2} + J_{\text{AF}}\sum_{\langle ij \rangle} \mathbf{S}_i \cdot \mathbf{S}_j,$$

$$D_{ij} = \sum_{\alpha\beta} t_{ij}^{\alpha\beta} \langle c_{i\alpha}^\dagger c_{j\beta} + \text{H.c.} \rangle.$$
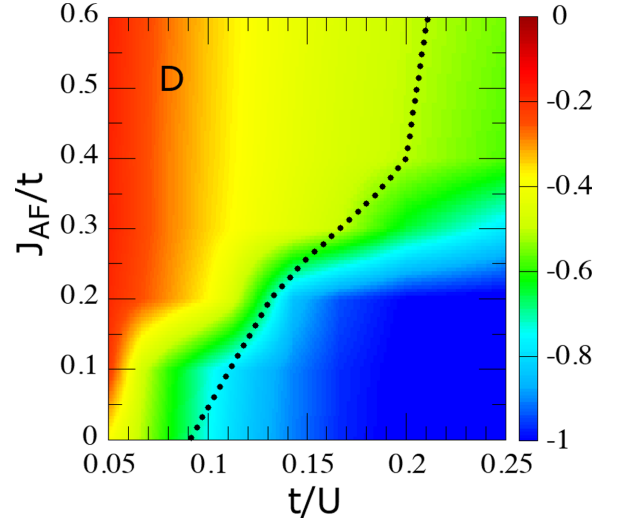


FIG. 9. The effective ferromagnetic exchange $D$ at $T = 0$ for varying $t/U$ and $J_{\text{AF}}/t$. The calculation and significance of this quantity is explained in the text. The MIT boundary is shown by dotted lines and coincides with the change from large to small values of $D$.

The role of the Hubbard interaction, acting through the orbital moment, is implicit in the model above. The $D_{ij}$ are supposed to be computed in backgrounds that include the $\Gamma_i$ as well as the AF coupling. Since the dependence of $D_{ij}$ on the magnetic and orbital state is not known, the model above does not have much predictive value. However, the thermally (and system) averaged $D_{ij}$, which we call just $D$, can serve to identify the origin of the changing magnetic character (see Fig. 9). It can also be related to direct measurables, e.g., (i) the spin stiffness (spin wave velocity), since the $D$ and $J_{\text{AF}}$ dictate this quantity, and (ii) the integrated optical weight, via the $f$-sum rule

$$\sum_{ij} D_{ij}\sqrt{(1 + \mathbf{S}_i \cdot \mathbf{S}_j)/2} \propto \int_0^\infty \sigma(\omega) d\omega \equiv n_{\text{eff}},$$

where $n_{\text{eff}}$, the integrated optical weight, is related to the effective carrier density. This can be roughly simplified to $D\sqrt{1 + m^2} \propto n_{\text{eff}}$, where we have approximated the spin average by $m^2$. The physics content of this is simple—reducing magnetization reduces the hopping ($D$) and the combination determines $n_{\text{eff}}$.

### A. The metal-insulator transition line

The role of $J_{\text{AF}}$ is to generate magnetic phase competition and reduce the ferromagnetic tendency by suppressing the kinetic energy. To set a convenient reference, the effective bond resolved kinetic energy $D$ at $J_{\text{AF}} = 0$ and $U \to 0$ is $\sim -t$. That allows us to set up three regimes.

(a) When $J_{\text{AF}} \ll D$, we essentially have a weakly renormalized FM ground state and $U_c$ is only modestly suppressed with respect to the $J_{\text{AF}} = 0$ value. For us this happens when $J_{\text{AF}} \lesssim 0.1t$. (b) In the interval $0.1t < J_{\text{AF}} < 0.4t$ the $U_c$ changes quickly, at $J_{\text{AF}} = 0.4t$ it is roughly half the value at $J_{\text{AF}} = 0$. (c) For $J_{\text{AF}} \gtrsim 0.4t$ the $U_c$ does not reduce any further since the magnetic ground state is completely disor-
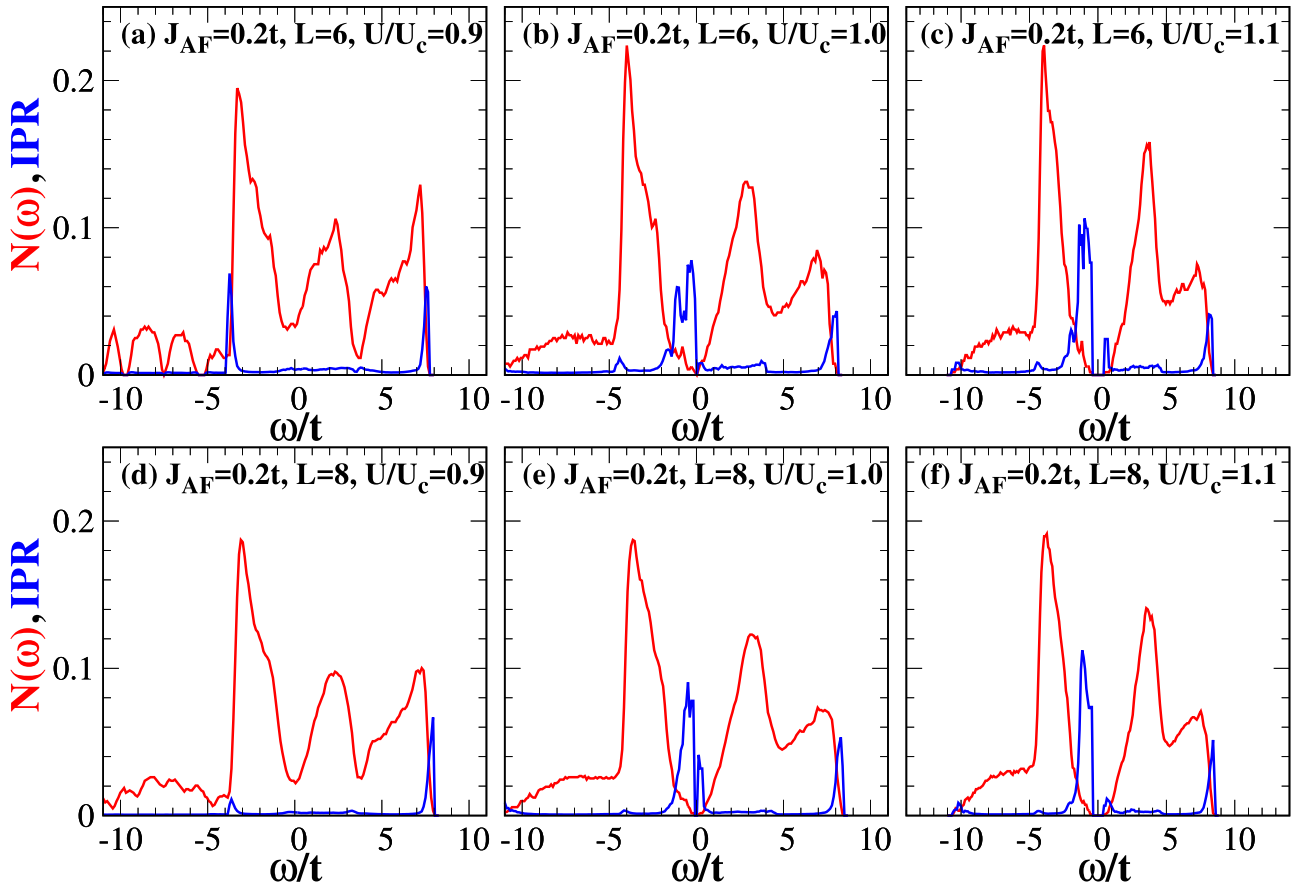
FIG. 10. Single particle DOS [$N(\omega)$] and inverse participation ratio (IPR) at $T = 0$ for the system sizes $L = 6$ (a)–(c) and $L = 8$ (d)–(f), for a selected choice of $J_{AF} = 0.2t$ at $U = 0.9U_c$, $U_c$, and $1.1U_c$, respectively.

dered and the magnetization cannot be suppressed any further. This shows up as the vertical asymptote of the MIT line in Fig. 1.

### B. The ferromagnet to "spin liquid" transition

The ferromagnet to spin liquid "transition" occurs along a line that we call $U_{mag}(J_{AF})$. There is some ambiguity in locating this line since within our parameter space the magnetization is always finite, if small. We set $M = 0.05$ as the S-F to S-L transition. Just as $U_c$ is dictated roughly by the competition between $U$ and $D$, $U_{mag}$ is decided by the competition between $J_{AF}$ and $D$.

### C. Anderson character of the Mott insulating phase

Increasing superexchange leads to progressively disordered spin and orbital backgrounds. As shown in Figs. 4(e) and 5(e) there is a parameter regime where there is an optical gap but no single particle gap (although there is a prominent pseudogap). An examination of the states near the Fermi energy in this regime, Fig. 10, shows that the low-energy states are localized, as characterized by significantly large values of inverse participation ratio (see the Appendix). These localized states are responsible for an insulating phase with finite optical gap, but no spectral gap. As $U$ is increased beyond $U_c$ a gap appears also in the single particle density of states. However,

the optical gap continues to remain larger than the single particle gap, and localized states still survive near the gap edges. This behavior is prominent at large $J_{AF}$ where the geometry of the pyrochlore lattice promotes spontaneous disorder. We characterize the behavior as "Anderson-like" in this strongly correlated system. The insulator close to the insulator-metal boundary should be properly characterized as an "Anderson-Mott insulator."

### V. CONCLUSION

In this paper we have studied the ground state properties of a two orbital Hubbard model with the electrons additionally strongly coupled to a background local moment—and the moments interacting antiferromagnetically among themselves. This Hubbard–double exchange–superexchange scenario, on the pyrochlore lattice, is the minimal model for the rare earth molybdates. We map out the ground state phase diagram via a simulated annealing based unrestricted Hartree-Fock calculation and establish the metal-insulator and ferromagnet-spin liquid transition boundaries. We provide the detailed structure factors, the density of states across the metal-insulator transition, and the optical conductivity, pointing out an increasing Anderson character to the notional Mott transition as the antiferromagnetic superexchange is increased. This effect should be readily observable in the high pressure experiments.

## APPENDIX: INVERSE PARTICIPATION RATIO AND ANDERSON-MOTT INSULATOR

Our measurement of spectral and optical gaps at the Fermi level reveals that unlike the naive expectation of them being equal, in the present system the magnitude of the optical gap exceeds that of the spectral gap. The observation can be attributed to "disorder free" Anderson-Mott localization, wherein the geometric frustration of the lattice gives rise to localization of the electrons. The corresponding single particle DOS exhibits accumulation of spectral weight at the gap edges, thereby reducing the spectral gap.

In order to ascertain the localizing tendency of the moments, we have calculated the inverse participation ratio (IPR) defined as

$$\text{IPR} = \sum_{i,\alpha,\sigma} \left| u_{\alpha,\sigma}^i \right|^4, \tag{A1}$$

where $u_{\alpha,\sigma}^i$ is the eigenvector corresponding to the eigenvalue $\epsilon_\alpha$. For an eigenstate $\psi_{i,\alpha}$ the localization length ($\xi_{\text{loc}}$) is related to the IPR as $\text{IPR} \propto 1/\xi_{\text{loc}}^2$. Thus, an increase in localization leads to reduced $\xi_{\text{loc}}$ and increase in IPR. In Fig. 10 we show the single particle DOS along with the corresponding IPR for a selected $J_{\text{AF}} = 0.2t$, as a function of increasing $U/t$

(normalized with respect to $U_c$, corresponding to the MIT at $J_{\text{AF}} = 0$). Furthermore, we have compared our results at two different system sizes which shows that our observations are robust against finite system size effects. Note that access to still larger system sizes is restricted by the computational expense.

Based on Fig. 10 we infer that for $U \gtrsim U_c$, the opening of the Mott gap at the Fermi level is accompanied by a progressive increase in IPR close to the gap edges. We quantify the observed localization in terms of the fraction of localized states, which is the ratio between the number of localized states and the total number of states. As a function of increasing $U/U_c$ the fraction of localized states for $L = 6$, varies as 0.165, 0.174, and 0.211 for $U = 0.9U_c$, $U_c$, and $1.1U_c$, respectively. For $L = 8$, the fraction of localized states changes to 0.154, 0.179, and 0.217 for $U = 0.9U_c$, $U_c$, and $1.1U_c$, respectively. This indicates that $U/t$ favors the localizing tendency of the moments.

Our result suggests the possibility of disorder free localization of single particle eigenstates aided by geometric frustration of the underlying lattice. It must however be noted that our current numerical framework does not take into account the effect of quantum fluctuations, which can lead to the dephasing of the single particle states. An analysis of the effect of quantum fluctuations on such frustration aided single particle localization is beyond the scope of this work. It is however expected that signatures of such localized states will survive at finite temperatures as well and will provide a possible mechanism to resolve the experimentally observed inequality between the spectral and optical gaps in geometrically frustrated pyrochlore lattices undergoing Mott transition.

[1] N. F. Mott, Proc. R. Soc. London Ser. A **62**, 416 (1949); *Metal-Insulator Transitions* (Taylor and Francis, London, 1990).

[2] M. Imada, A. Fujimori, and Y. Tokura, Rev. Mod. Phys. **70**, 1039 (1998).

[3] J. E. Hirsch, Phys. Rev. B **31**, 4403 (1985).

[4] L. Balents, Nature (London) **464**, 199 (2010).

[5] Y. Imai and N. Kawakami, Phys. Rev. B **65**, 233103 (2002).

[6] O. Parcollet, G. Biroli, and G. Kotliar, Phys. Rev. Lett. **92**, 226402 (2004).

[7] B. Kyung and A.-M. S. Tremblay, Phys. Rev. Lett. **97**, 046402 (2006).

[8] T. Ohashi, T. Momoi, H. Tsunetsugu, and N. Kawakami, Phys. Rev. Lett. **100**, 076402 (2008).

[9] A. Wietek, R. Rossi, F. Šimkovic, M. Klett, P. Hansmann, M. Ferrero, E. M. Stoudenmire, T. Schäfer, and A. Georges, Phys. Rev. X **11**, 041013 (2021).

[10] P. W. Anderson, Mater. Res. Bull. **8**, 153 (1973).

[11] Y. Shimizu, K. Miyagawa, K. Kanoda, M. Maesato, and G. Saito, Phys. Rev. Lett. **91**, 107001 (2003).

[12] M. Yamashita, N. Nakata, Y. Kasahara, T. Sasaki, N. Yoneyama, N. Kobayashi, S. Fujimoto, T. Shibauchi, and Y. Matsuda, Nat. Phys. **5**, 44 (2009).

[13] K. Kanoda and R. Kato, Annu. Rev. Condens. Matter Phys. **2**, 167 (2011).

[14] B. J. Powell and R. H. McKenzie, Rep. Prog. Phys. **74**, 056501 (2011).

[15] S. Imajo, N. Kato, R. J. Marckwardt, E. Yesil, H. Akutsu, and Y. Nakazawa, Phys. Rev. B **105**, 125130 (2022).

[16] Y. Imai, N. Kawakami, and H. Tsunetsugu, Phys. Rev. B **68**, 195103 (2003).

[17] N. Bulut, W. Koshibae, and S. Maekawa, Phys. Rev. Lett. **95**, 037001 (2005).

[18] T. Ohashi, N. Kawakami, and H. Tsunetsugu, Phys. Rev. Lett. **97**, 066401 (2006).

[19] A. Yamada, K. Seki, R. Eder, and Y. Ohta, Phys. Rev. B **83**, 195127 (2011).

[20] T. Kita, T. Ohashi, and N. Kawakami, Phys. Rev. B **87**, 155119 (2013).

[21] R-Y. Sun and Z. Zhu, Phys. Rev. B **104**, L121118 (2021).

[22] J. Kaufmann, K. Steiner, R. T. Scalettar, K. Held, and O. Janson, Phys. Rev. B **104**, 165127 (2021).

[23] J. S. Gardner, M. J. P. Gingras, and J. E. Greedan, Rev. Mod. Phys. **82**, 53 (2010).

[24] W. Witczak-Krempa, G. Chen, Y. B. Kim, and L. Balents, Annu. Rev. Condens. Matter Phys. **5**, 57 (2014).

[25] J. G. Rau, E. K.-H. Lee, and H.-Y. Kee, Annu. Rev. Condens. Matter Phys. **7**, 195 (2016).

[26] J. G. Rau and M. J. P. Gingras, Annu. Rev. Condens. Matter Phys. **10**, 357 (2019).

[27] P. A. Lee, J. Phys.: Conf. Ser. **529**, 012001 (2014).

[28] M. B. Salamon and M. Jaime, Rev. Mod. Phys. **73**, 583 (2001).

[29] B. D. Gaulin, J. N. Reimers, T. E. Mason, J. E. Greedan, and Z. Tun, Phys. Rev. Lett. **69**, 3244 (1992).

[30] M. J. P. Gingras, C. V. Stager, N. P. Raju, B. D. Gaulin, and J. E. Greedan, Phys. Rev. Lett. **78**, 947 (1997).

[31] Y. Taguchi and Y. Tokura, Phys. Rev. B **60**, 10280 (1999).

[32] I. Kézsmárki, N. Hanasaki, K. Watanabe, S. Iguchi, Y. Taguchi, S. Miyasaka, and Y. Tokura, Phys. Rev. B **73**, 125122 (2006).

[33] S. Iguchi, N. Hanasaki, M. Kinuhara, N. Takeshita, C. Terakura, Y. Taguchi, H. Takagi, and Y. Tokura, Phys. Rev. Lett. **102**, 136407 (2009).

[34] D. Yanagishima and Y. Maeno, J. Phys. Soc. Jpn. **70**, 2880 (2001).

[35] K. Matsuhira, M. Wakeshima, Y. Hinatsu, and S. Takagi, J. Phys. Soc. Jpn. **80**, 094701 (2011).

[36] M. Sakata, T. Kagayama, K. Shimizu, K. Matsuhira, S. Takagi, M. Wakeshima, and Y. Hinatsu, Phys. Rev. B **83**, 041102(R) (2011).

[37] F. F. Tafti, J. J. Ishikawa, A. McCollam, S. Nakatsuji, and S. R. Julian, Phys. Rev. B **85**, 205104 (2012).

[38] I. V. Solovyev, Phys. Rev. B **67**, 174406 (2003).

[39] B. J. Kim, H. Jin, S. J. Moon, J.-Y. Kim, B.-G. Park, C. S. Leem, J. Yu, T. W. Noh, C. Kim, S.-J. Oh, J.-H. Park, V. Durairaj, G. Cao, and E. Rotenberg, Phys. Rev. Lett. **101**, 076402 (2008).

[40] K. Tomiyasu, K. Matsuhira, K. Iwasa, M. Watahiki, S. Takagi, M. Wakeshima, Y. Hinatsu, M. Yokoyama, K. Ohoyama, and K. Yamada, J. Phys. Soc. Jpn. **81**, 034709 (2012).

[41] H. Sagayama, D. Uematsu, T. Arima, K. Sugimoto, J. J. Ishikawa, E. O'Farrell, and S. Nakatsuji, Phys. Rev. B **87**, 100403(R) (2013).

[42] S. M. Disseler, Phys. Rev. B **89**, 140413(R) (2014).

[43] J. E. Greedan, M. Sato, N. Ali, and W. R. Datars, J. Solid State Chem. **68**, 300 (1987).

[44] K. Miyoshi, K. Honda, T. Yamashita, K. Fujiwara, and J. Takeuchi, J. Magn. Magn. Mater. **226-230**, 898 (2001).

[45] I. Kézsmárki, N. Hanasaki, D. Hashimoto, S. Iguchi, Y. Taguchi, S. Miyasaka, and Y. Tokura, Phys. Rev. Lett. **93**, 266401 (2004).

[46] N. Ali, M. P. Hill, S. Labroo, and J. E. Greedan, J. Solid State Chem. **83**, 178 (1989).

[47] N. Ali, P. Hill, X. Zhang, and F. Willis, J. Alloys Compd. **181**, 281 (1992).

[48] T. Katsufuji, H. Y. Hwang, and S. W. Cheong, Phys. Rev. Lett. **84**, 1998 (2000).

[49] Y. Taguchi, Y. Oohara, H. Yoshizawa, N. Nagaosa, and Y. Tokura, Science **291**, 2573 (2001).

[50] Y. Taguchi, T. Sasaki, S. Awaji, Y. Iwasa, T. Tayama, T. Sakakibara, S. Iguchi, T. Ito, and Y. Tokura, Phys. Rev. Lett. **90**, 257202 (2003).

[51] S. Iguchi, N. Hanasaki, and Y. Tokura, Phys. Rev. Lett. **99**, 077202 (2007).

[52] K. Ueda, S. Iguchi, T. Suzuki, S. Ishiwata, Y. Taguchi, and Y. Tokura, Phys. Rev. Lett. **108**, 156601 (2012).

[53] N. Hanasaki, M. Kinuhara, I. Kézsmárki, S. Iguchi, S. Miyasaka, N. Takeshita, C. Terakura, H. Takagi, and Y. Tokura, Phys. Rev. Lett. **96**, 116403 (2006).

[54] C. Castellano, G. Berti, F. Rubio-Marcos, G. Lamura, S. Sanna, E. Salas-Colera, A. Brambilla, Á. Muñoz-Noval, L. Duò, and F. Demartin, J. Alloys Compd. **723**, 327 (2017).

[55] M. Hirschberger, Y. Kaneko, L. Spitz, T. Nakajima, Y. Taguchi, and Y. Tokura, Phys. Rev. B **104**, 024436 (2021).

[56] M. Hirschberger, Y. Nomura, H. Mitamura, A. Miyake, T. Koretsune, Y. Kaneko, L. Spitz, Y. Taguchi, A. Matsuo, K. Kindo, R. Arita, M. Tokunaga, and Y. Tokura, Phys. Rev. B **103**, L041111 (2021).

[57] T. E. Saunders and J. T. Chalker, Phys. Rev. Lett. **98**, 157201 (2007).

[58] H. Shinaoka, Y. Tomita, and Y. Motome, Phys. Rev. Lett. **107**, 047204 (2011); H. Shinaoka, Phys. Rev. B **90**, 165119 (2014).

[59] Y. Motome and N. Furukawa, J. Phys.: Conf. Ser. **320**, 012060 (2011).

[60] Y. Motome and N. Furukawa, Phys. Rev. Lett. **104**, 106407 (2010); Y. Motome, Phys. Rev. B **82**, 060407(R) (2010).

[61] A. Georges, G. Kotliar, W. Krauth, and M. J. Rozenberg, Rev. Mod. Phys. **68**, 13 (1996).

[62] J. Hubbard, Phys. Rev. Lett. **3**, 77 (1959).

[63] J. Hubbard, Phys. Rev. B **19**, 2626 (1979).

[64] H. J. Schulz, Phys. Rev. Lett. **65**, 2462 (1990).

[65] P. Arve, G. Bertsch, B. Lauritzen, and G. Puddu, Ann. Phys. **183**, 309 (1988).

[66] B. Lauritzen, P. Arve, and G. F. Bertsch, Phys. Rev. Lett. **61**, 2835 (1988).

[67] M. Mayr, G. Alvarez, C. Sen, and E. Dagotto, Phys. Rev. Lett. **94**, 217001 (2005).

[68] Y. Dubi, Y. Meir, and Y. Avishai, Nature (London) **449**, 876 (2007).

[69] M. Karmakar and P. Majumdar, Phys. Rev. A **93**, 053609 (2016).

[70] N. Swain and M. Karmakar, Phys. Rev. Res. **2**, 023136 (2020).

[71] R. Tiwari and P. Majumdar, Europhys. Lett. **108**, 27007 (2014).

[72] N. Swain, R. Tiwari, and P. Majumdar, Phys. Rev. B **94**, 155119 (2016).

[73] S. Kumar and P. Majumdar, Eur. Phys. J. B **50**, 571 (2006).

[74] S. Kumar and P. Majumdar, Eur. Phys. J. B **46**, 315 (2005).